We are IntechOpen, the world's leading publisher of Open Access books Built by scientists, for scientists

4,800
Open access books available

122,000
International authors and editors

135M
Downloads

Our authors are among the

154
Countries delivered to

TOP 1%
most cited scientists

12.2%
Contributors from top 500 universities

WEB OF SCIENCE™

Selection of our books indexed in the Book Citation Index in Web of Science™ Core Collection (BKCI)

Interested in publishing with us?
Contact book.department@intechopen.com

Numbers displayed above are based on latest data collected.
For more information visit www.intechopen.com

5

Local Structure of Relaxor Dielectric Ceramics

Yun Liu and Ray L. Withers
The Australian National University
Australia

1. Introduction

The electric field and frequency dependence of the dielectric permittivities of relaxor dielectrics makes them promising tuneable microwave component materials and gives rise to numerous potential applications, especially in the fields of electronics and telecommunications technologies. Relaxors of this type have been known for over half a century. The relaxation mechanisms underlying their unique dielectric behaviour, however, are still far from well understood. This lack of understanding is a significant impediment to the further development and optimization of their desirable dielectric properties (high dielectric constants, low dielectric losses and high field tuneabilities). Because such functional relaxors are almost invariably chemically and/or displacively disordered, an understanding of their local nanoscale crystal structure is an important starting point to gain a better understanding of their intrinsic dielectric properties.

Conventional Bragg scattering diffraction techniques, whether obtained via X-ray diffraction (XRD), neutron diffraction or electron diffraction, contain only 1-body information on the time and space averaged crystal structure as a result of the assumption of a regularly repeating real space unit cell and its corollary, sharp Bragg reflections only in reciprocal space (see *e.g.* Fig.1a). Correlated chemical and/or displacive deviations from that average structure *i.e.* information on local order, on the other hand, gives rise to additional, usually much weaker, structured diffuse scattering in addition to the strong Bragg reflections of the underlying average structure (see *e.g.* Fig.1b). The detection and reciprocal space mapping of such structured diffuse intensity distributions is an important step towards a structural understanding of the chemical and/or displacive disorder responsible and the relationship that this local order may, or may not, have with electric dipoles and intrinsic dielectric relaxation behaviour. Ultimately, real space modelling and fitting to the observed diffuse distribution is required in order to extract the local ordering responsible.

Electron diffraction is ideally suited to the detection and mapping task as a result of the strength of the interaction between fast electrons and matter, the ability to record planar cross-sections of reciprocal space from localized real space regions coupled with the ability to tilt over large angular ranges enabling the systematic exploration of reciprocal space. The strong interaction of electrons with matter, however, does mean that the effects of multiple scattering and dynamical diffraction need to be borne in mind, in particular at major zone axis orientations. It is thus often quite useful to deliberately take *off-axis* electron diffraction patterns in order to minimize the effects of multiple scattering. By such methods, useful and reliable structural information can be extracted from such data.

Figure 1a, for example, shows a typical <-110> zone axis electron diffraction pattern (EDP) of $CaCu_3Ti_4O_{12}$, a giant dielectric constant material. Only sharp Bragg reflections are observed, entirely compatible with the reported *Im*-3, non-polar, average structure space group symmetry of this material. On tilting away from this exact zone axis orientation, however, keeping an <002>* systematic row excited and choosing a longer exposure time, the weak but quite reproducible, highly structured diffuse intensity distribution shown in Fig.1b becomes apparent in this compound. Transverse polarized diffuse streaking of this type continues to exist no matter how far one tilts around the <002>* direction showing that the diffuse distribution takes the form of sheets of diffuse intensity perpendicular to the three <001> real space directions (Liu et al., 2005). It is shown in their work that this observed diffuse distribution results from correlated off-center displacements of Ti ions along one-dimensional <001> columns. While the giant dielectric constant of this material has now been shown to arise from an extrinsic rather than intrinsic origin, it nonetheless remains of interest that $CaCu_3Ti_4O_{12}$ is an incipient ferroelectric.

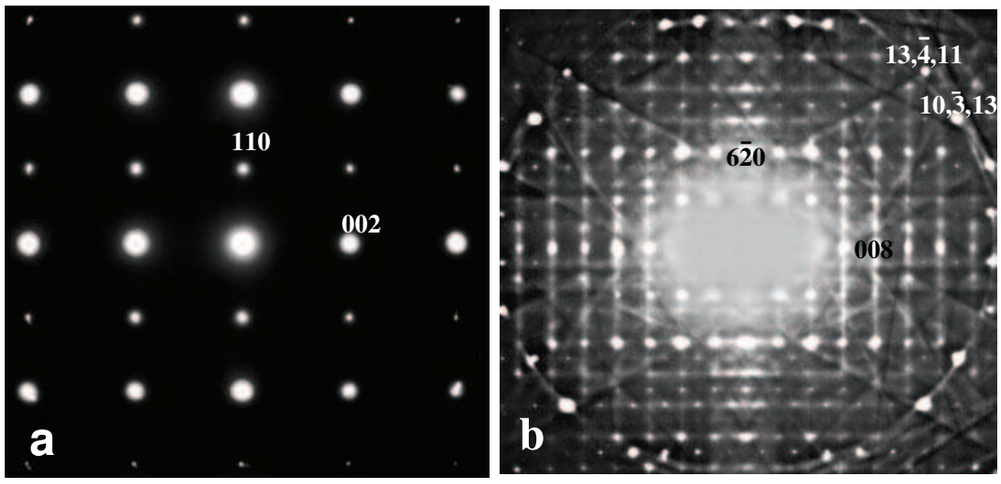

Fig. 1. Typical <110> (a) and close to <130> zone axis electron diffraction patterns of $CaCu_3Ti_4O_{12}$ ceramic (Liu et al, 2005)

For the remainder of this chapter, we will take the family of bismuth-based niobate pyrochlore electroceramics as an example to show how local nanoscale structure affects dielectric relaxation properties even though they have essentially the same average structures.

2. Average structure and dielectric properties of Bi-based niobate pyrochlores

The ideal $A_2B_2O_7$ cubic pyrochlore structure type (see Fig.2a) has space group symmetry *Fd-3m* (with *A* on *16d* at 1/2, 1/2, 1/2; *B* on *16c* at 000; O on *48f* at x, 1/8, 1/8 and O' on *8b* at 3/8, 3/8, 3/8, origin choice 2; note that x is typically ~ 0.30-0.34). It consists of two intergrown substructures: an $O'A_2$ tetrahedral corner-connected, anti-cristobalite type substructure (see Fig. 2b) and a B_2O_6 octahedral corner-connected substructure (see Fig. 2c). These two component substructures then intergrow to form the overall pyrochlore structure type (see Fig.2a).

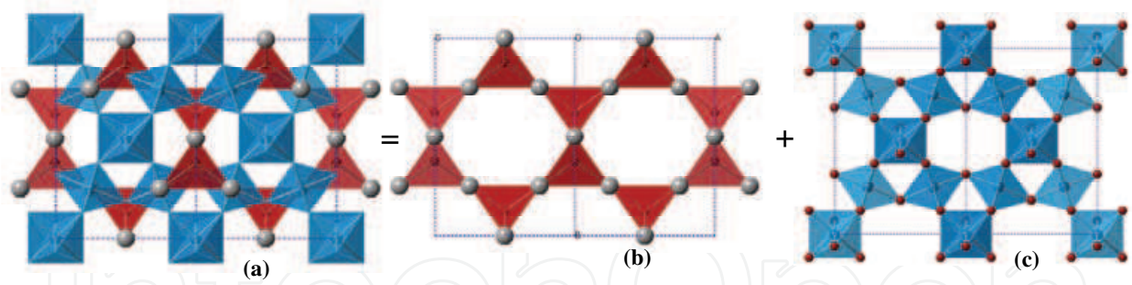

Fig. 2. Ideal cubic pyrochlore structure type (a) described by two constituent network substructures: corner-connected, oxygen-centered O′ A_2 tetrahedral anti-cristobalite structure (b) and corner connected, cation-centered BO_6 octahedral network (c).

While the bonding is strongest within each component sub-structure, the two sub-structures are not independent of one another. The *A* cations of the anti-cristobalite type substructure, in particular, are bonded reasonably strongly to the O ions of the B_2O_6 octahedral substructure. Breaking the ideal cubic pyrochlore structure up in this way is nonetheless a valid and quite useful means of investigating the crystal chemistry of the overall structure.

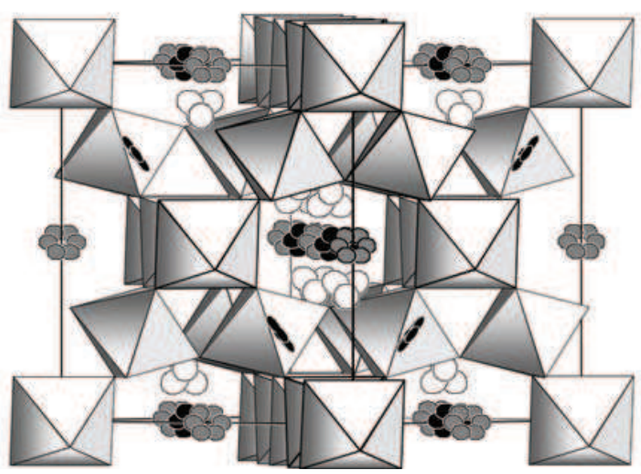

Fig. 3. The displacively disordered average structure of $Bi_{1.667}Mg_{0.70}Nb_{1.52}O_7$ projected along a close to <110> direction (see Nguyen et al., (2007a) for details). The corner-connected octahedral array represents the $(Mg_{0.24}Nb_{0.76})_2O_6$ octahedral sub-structure. The toroids of flat ellipsoids represents the six equivalent *96h A* site positions of the O′$(Bi_{0.833}Mg_{0.11})_2$ sub-structure. The tetrahedral clusters of ellipsoids represents the four equivalent 32*e* site positions for the displaced O′ oxygens.

The larger eight-coordinate *A* site of bismuth-based niobate pyrochlores is occupied mainly by Bi^{3+} ions and the smaller octahedral *B* site mainly by Nb^{5+} ions as would be expected. Surprisingly, however, a large and growing family of cubic pyrochlores have now been shown to exist with nominally too small M^{2+} metal ions, *M* = Zn, Ni, Mg *etc.*, occupying up to 25% of the large *A* cation sites. The nominal stoichiometry of such bismuth-based niobate pyrochlores is $(Bi_{1.5}M_{0.5})(M_{0.5}Nb_{1.5})O_7$. Examples of this type include $(Bi_{1.5}Zn_{0.5})(Zn_{0.5}Nb_{1.5})O_7$ (BZN), $(Bi_{1.5}Ni_{0.5})(Ni_{0.5}Nb_{1.5})O_7$ (BNN) and $(Bi_{1.5}Mg_{0.5})(Mg_{0.5}Nb_{1.5})O_7$ (BMN). Alternatively,

three-valent metal ions M^{3+}, can half occupy the pyrochlore *B* site giving rise to bismuth-based niobate pyrochlores of nominal stoichiometry $(Bi_2)(M_1Nb_1)O_7$. Examples of this type include Bi_2InNbO_7 (BIN), Bi_2ScNbO_7 (BSN) and Bi_2FeNbO_7 (BFN) *etc*. Careful phase analysis studies of many such systems, however, shows that there are often vacancies on the pyrochlore *A* site and associated oxygen ion vacancies as well (Levin et al., 2002; Withers et al., 2004). Clearly there is considerable scope for local chemical and associated displacive disorder in these systems.

Average structure refinements of these bismuth-based niobate pyrochlores shows that they are all of the same cubic pyrochlore average structure type with similar cubic lattice parameters [a = 10.5465(9)-10.5633(9) Å for BZN(Levin et al., 2002; Withers et al., 2004), a = 10.5354(2) Å for BNN and a = 10.5607 (5) Å for BMN (Nguyen et al., 2007b), a = 10.5255(1) Å for BFN (Somphon et al., 2006), a = 10.792(2) Å for BIN and a = 10.660(9) Å for BSN (Liu et al., 2009)]. In addition, they all show considerable displacive disorder in the O'A_2 tetrahedral structure, usually modelled in terms of a split atom approach (see Fig.3 above). The nature of this disorder, however, is unclear from these average structure refinements. Do the disordered atoms hop independently of one another or do they move together in a correlated fashion and how might this affect the formation of electric dipoles and their dielectric behaviour?

From the dielectric properties point of view, frequency dispersive behaviour is clearly apparent and always observed in both the dielectric permittivity and dielectric loss spectra of these materials (see *e.g.* Fig.4) *i.e.* all of these bismuth-based niobate pryochlores are relaxor dielectrics.

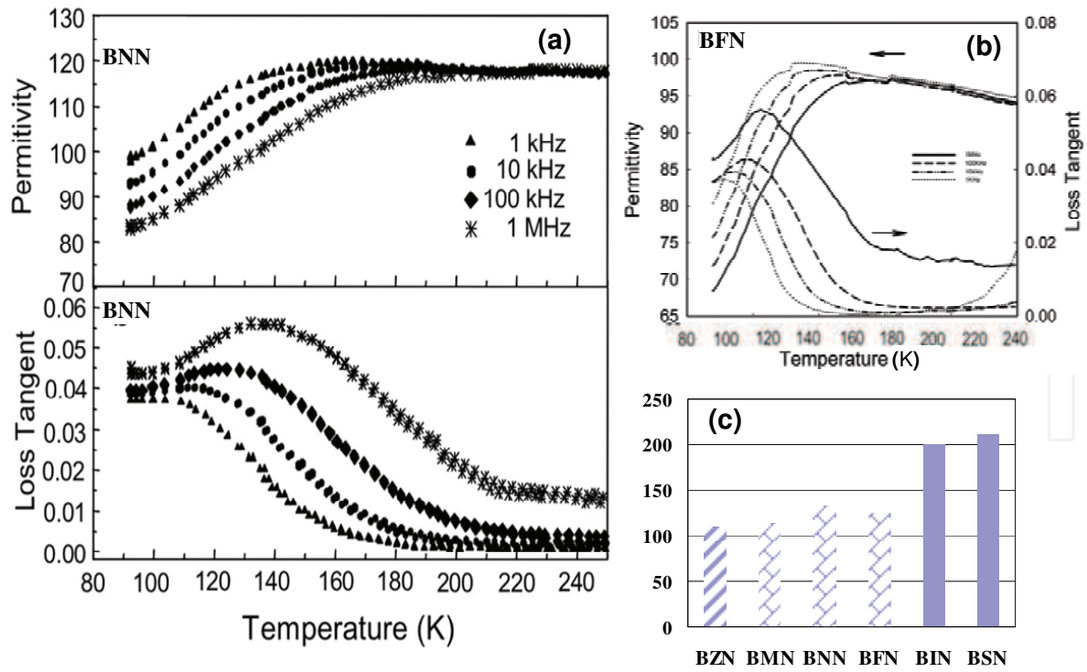

Fig. 4. Temperature dependece of the dielectric permittivity and loss tangent of BNN (a) and BFN (b) as well as the maximum temperature of loss tangent of Bi-based niobate pyrochlores (c) measured at 1 MHz.

Fig.4, for example, shows the temperature dependence of the dielectric permittivity and dielectric loss tangent of (a) BNN and (b) BFN at different frequencies (1 kHz, 10 kHz, 100 kHz and 1 MHz). It is noteworthy that the dielectric loss tangent of BNN first increases with decreasing temperature until a peak in the dielectric loss tangent (at T_m) and then decreases until it flattens off at a somewhat lower temperature into an apparent plateau region. Indeed, the dielectric loss tangent curve at 1 kHz is so flat at low temperature that a prior peak in the dielectric loss tangent is not distinguishable. It appears then that there may well be at least two peaks in the dielectric loss tangent in the case of BNN. Such asymmetric dielectric loss tangent curves such as that observed for BNN but not for BZN, suggest that BNN may well have different local structural order and hence a different dielectric relaxation mechanism to BZN. A similar trend is also observed in the cases of BMN (Nguyen et al., 2007a) and BFN (Fig. 4b).

Note that the dielectric permittivity is relatively flat at higher temperatures, but exhibits a typical step-like slowing down on cooling. Such behaviour is indicative of displacive motion requiring thermally activated hopping over a potential barrier, which then freezes out at a sufficiently low temperature. The frequency dependence of the peak position in the dielectric loss curve (see Fig.4), following a previous approach (Kamba et al., 2002; Nino et al., 2001), can in general be modelled using either the basic Arrhenius type equation $f_r = f_0 \exp(-Ea / kT)$ or the Vogel–Fulcher equation $f_r = f_0 \exp[-Ea / k(T - T_f)]$. Here f_r is the measuring frequency, f_0 is the relaxation frequency at infinite temperature, E_a represents an activation energy, k is the Boltzmann constant, T is the temperature of the peak position in the dielectric loss curve at the particular measuring frequency and T_f represents the freezing temperature of the relaxation. The Arrhenius type equation should be valid provided that the potential barrier is uniform for all hopping charges and that the charges hop independently of one another. The Vogel–Fulcher equation, however, also takes into consideration the possibility of correlated hopping.

It is noteworthy that the peak in the dielectric loss as a function of frequency is shifted to significantly higher temperatures in the cases of BIN and BSN relative to the other Bi-based pyrochlores *e.g.* T_m at 1 MHz = 211 K for BSN and 200 K for BIN but only 133 K for BNN, 125 K for BFN, 114 K for BMN and ~ 110 K for BZN (see Fig. 4c). The differing temperatures of the peak in the dielectric loss tangent as well its different behaviour below T_m from one Bi-based pyrochlore system to the next suggests the existence of different dipole activation energies, different local structural order and consequently different relaxation mechanisms in these compounds even through they have the same average structure.

2.1 $(Bi_{1.5}Zn_{0.5})(Zn_{0.5}Nb_{1.5})O_7$ (BZN) pyrochlore

2.1.1 Local structure of BZN

Figure 5 shows close to (a) <001>, (b) <118> and (c) <551> zone axis electron diffraction patterns typical of BZN collected at room temperature along with Monte Carlo simulated diffraction patterns at the same zone axis orientations in (d)-(f). No diffuse scattering was observed at either the exact <100> or <110> zone axis orientations. On tilting away from these exact zone axis orientations, however, a characteristic, highly structured and quite reproducible diffuse intensity distribution was always observed, as apparent from Fig.5. Fig.5b, for example, shows an electron diffraction pattern collected by tilting (~10°) away from the <001> orientation keeping a <2-20>* systematic row excited. Likewise, Fig.5c is

obtained by tilting ~9° away from the exact <110> zone axis orientation keeping a <2-20>* systematic row excited.

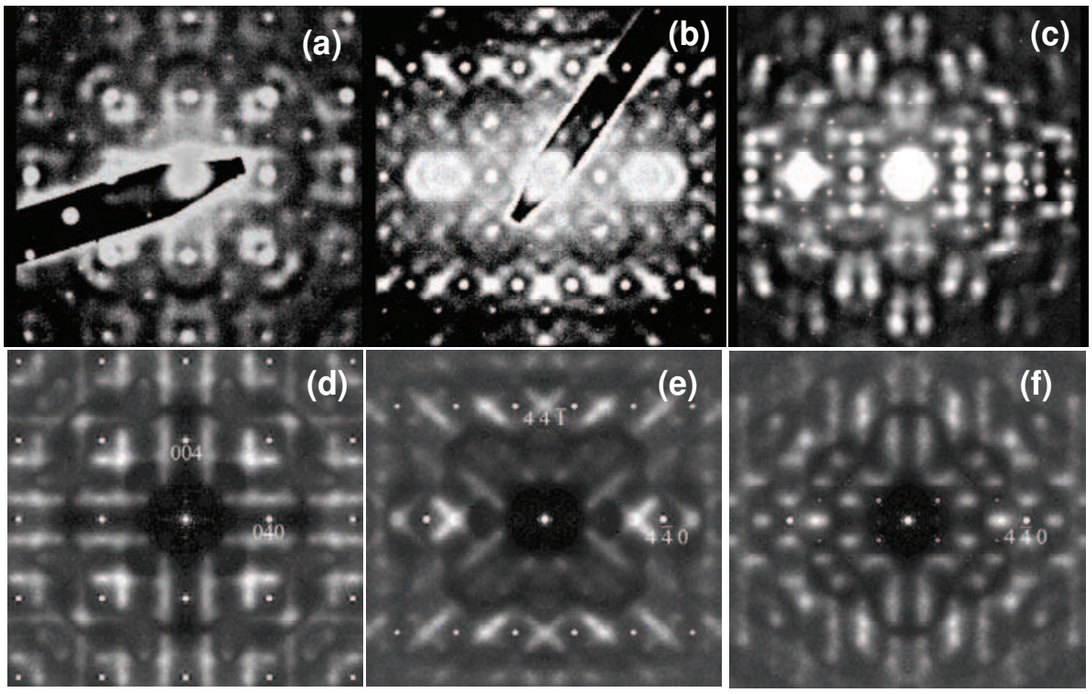

Fig. 5. Typical <001> (a), <118>(b) and <551> (c) zone axis electron diffraction patterns of BZN and corresponding Monte Carlo simulation result (d-f). See detail in ref (Withers et al., 2004).

Note that tilting progressively away from the <001> orientation shows the intensity of the diffuse streaking along the <w01>* and <0w1>* directions of reciprocal space become more limited, suggesting that the diffuse streaking occurs in one-dimensional lines running simultaneously along all three <001>* directions of reciprocal space. The intensity of the <801>* diffuse streaking is strongest along the <801>* direction of reciprocal space itself, however it is virtually absent along the orthogonal direction. This is due to a substantial 'size effect' contribution (Butler et al., 1992) that leads to the asymmetry of the diffuse distribution surrounding Bragg reflections e.g. <044>* in Fig. 5a [see ref (Withers et al., 2004) for details]. Furthermore, the diffuse streaks only run through the G±<001>* type positions and not through the Fd3m allowed Bragg reflections. The reciprocal space positioning of the observed diffuse distribution thus appears to be given by **G**±[10*l*]*, **G**±[*h*10]* and **G**±[0*k*1]* respectively, where **G** represents an allowed parent pyrochlore Bragg reflection. The strong diffuse blobs at the **G**±<001>* positions of reciprocal space (such as <441>* in Fig. 5b) originates from the intersection of two such diffuse streaks at this point. Now the question becomes what is the origin of this structured diffuse intensity distribution.

The bond valence approach is a powerful empirical tool which gives the relationship between the bond length and strength of chemical bonds between cations and anions and can be used for the assessment and prediction of structural stability, in particular disordered local structure. Using this approach, the apparent valence (AV) or bond valence sum (V(*A*))

of a cation A in terms of its bonds to all its coordinating anions X is given by $V(A) = \sum_X S_{A-X} = \sum_x \exp[(R_0 - R_{A-X})/b]$ where R_0 and b (= 0.37 Å) are empirical parameters, available from the list in *e.g.* ref (Brese & O'Keeffe, 1991). For this bond valence sum calculation, a nominal stoichiometry of $(Bi_{1.5}Zn_{0.5})(Zn_{0.5}Nb_{1.5})O_7$ is assumed, ignoring the known slight non-stoichiometry (Levin et al., 2002; Withers et al., 2004). The average occupancy of the octahedral B site is thus $^3/_4$ Nb + $^1/_4$ Zn while that of the A site is $^3/_4$ Bi + $^1/_4$ Zn. Consider firstly the B_2O_6, octahedral corner-connected sub-structure (see Fig.2c). For a Nb-centred octahedra, the expected metal-oxygen bond length is then given by R_{Nb-O} = 1.911 – 0.37 ln(5/6) Å = 1.9785 Å using $R_0(Nb^{5+}\text{-}O^{2-})$ = 1.911 Å (Brese & O'Keeffe, 1991). Likewise, for a Zn-centred octahedra, the expected metal-oxygen bond length is given by R_{Zn-O} = 1.704 – 0.37 ln(2/6) = 2.1105 Å, using $R_0(Zn^{2+}\text{-}O^{2-})$ = 1.704 Å(Brese & O'Keeffe, 1991). The average metal ion-oxygen bond length should then be $^3/_4$ x 1.9785 + $^1/_4$ x 2.1105 = 2.0115 Å which is very close to the refined value of 2.0065 Å (Levin et al., 2002). The two predicted ideal bond lengths are each quite close to the average R_{B-O} distance, with the ideal Nb-O bond length being slightly smaller than the average and the ideal Zn-O bond length being slightly larger than the average. Therefore, local displacements of the B and O sites away from their refined average positions can be expected to be relatively small whatever the local chemistry. Locally, one would expect Nb^{5+}-centred octahedra to shrink slightly by sucking in the 6 surrounding O ions from the average distance of 2.01 Å to the ideal distance of 1.91 Å while Zn^{2+}-centred octahedron could be expected to expand slightly slightly from the average distance of 2.01 Å to the ideal distance of 2.11 Å. These displacements are so small that we can largely neglect the contribution of the B_2O_6 sub-structure to the observed diffuse intensity.

A	B	AV(A)	AV(B)	AV(O)	AV(O')
Bi	Nb	2.461	4.635	1.969	2.377
Bi	Zn	2.461	2.649	1.307	2.3777
Zn	Nb	0.858	4.635	1.693	0.828
Zn	Zn	0.858	2.649	1.031	0.828
	[Bi_4]	[Bi_3Zn]	[Bi_2Zn_2]	[$BiZn_3$]	[Zn_4]
AV(O')[A_4]	2.377	1.990	1.603	1.215	0.828
	[Bi_2Nb_2]	[Bi_2NbZn]	[$BiZnNb_2$]	[BiZnNbZn]	
AV(O)[A_2B_2]	1.969	1.638	1.831	1.500	

Table 1. Bond Valence Sums (AV) for the BZN average structure, O' and O dependent on [A_4] and [A_2B_2] {Withers, 2004}

Now consider the O'A_2 anti-cristobalite substructure (see Fig.2b and Table 1 above). Each O' anion is tetrahedrally coordinated to 4 A cations at an average distance $R_{O'-A} = \sqrt{3}/8\ a$ = 2.287 Å. Using the same type of bond valence argument given above [see ref. (Withers et al., 2004) for details], one would expect an ideal $R_{O'-Bi}$ distance of 2.3505 Å if the O' ion is surrounded by 4 Bi's and an ideal $R_{O'-Zn}$ distance of 1.9605 Å if the O' ion is surrounded by 4 Zn's. Note that this time these two bond lengths differ quite significantly from each other and from the average O'-A distance. Thus considerable local strain relaxation of the O'A_2

sub-structure can be expected associated with the local distribution of Bi^{3+} and Zn^{2+} on the *A* sites. This strongly suggests that the disorder and subsequent structural relaxation in the O'A_2 substructure is largely responsible for the observed diffuse intensity distribution.
The best way to minimize this local strain relaxation is for the stoichiometry of the O'A_4 tetrahedra to have the average stoichiometry wherever possible *i.e.* O'Bi_3Zn so that the 2 O' ions on either side of a central Zn^{2+} ion can simultaneously contract in towards it along a local <111> direction and away from the neighbouring Bi^{3+} ions. From Table 1, the O' ion can be relatively happily bonded only when it is surrounded by 3 Bi's and 1 Zn, *i.e.* from the local crystal chemical point of view it is of paramount importance wherever possible to achieve the average composition of O'Bi_3Zn in each local tetrahedron (see Table 1 and Fig. 6). There are only two distinct types of inter-tetrahedral Zn-Zn separation vectors possible (shown in Figs.6a and b). The first is of $^1/_4$ <112> type (shown in Fig.6a) in which neighbouring O' ions centring the O'Bi_3Zn tetrahedra must shift directly towards the significantly under-bonded Zn ions (solid line arrows). The Bi ions in the same tetrahedron cannot afford to lose the valence contribution from these O' ions, however, and hence will seek to follow the induced O' ion shifts. This induces shifts of the Bi ions perpendicular to the local O'-Bi-O' axis towards two of the six surrounding equatorial O ions (see Fig. 6c). The only other possible type is of $^1/_2$ <110> type Zn-Zn separation. Such a Zn-Zn separation (Fig. 6b), however, does not allow the Bi ions to follow the O' shifts and hence leads to a significantly under-bonded Bi ion and thus is energetically extremely unfavourable (see ref. (Withers et al., 2004) for details). This provides a clear crystal chemical rationale as to why $^1/_4$ <112> type Zn-Zn separation vectors should be strongly favoured and $^1/_2$ <110> type Zn-Zn separation vectors completely avoided in BZN-related pyrochlores. Finally, the difference in size between the Bi^{3+} and Zn^{2+} ions also leads to an additional "size effect" relaxation within each tetrahedron. From Table 1, it is apparent that Bi cations in the pyrochlore *A* site are always underbonded. Thus, when an O' ion moves towards a Zn ion (see Figs. 6a and c), the remaining three Bi cations in the tetrahedron will attempt to follow, consequently shortening the local Zn-Bi separation distance and lengthening the local Bi-Bi separation distance.

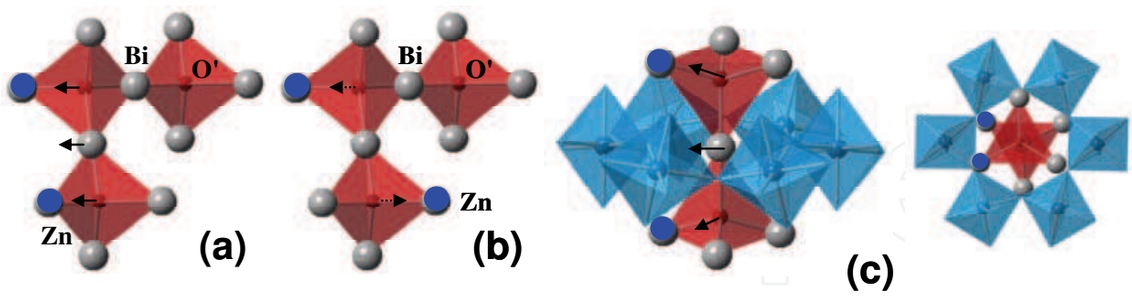

Fig. 6. (a) and (b) two possible arrangements of inter-tetrahedral Zn-Zn separation, and (c) the hexagonal prismatic enviroment of the *A* cations in the pyrochlore average structure type in projection along <1,-1,0> and <111> respectively. Zn ions: blue, Bi: grey. The displacements of the O′ ions (initially centring the two O′Bi_3Zn tetrahedra shown) towards the Zn ions in each tetrahedra are shown by the solid lines while the induced shift of the central Bi ion represented by the dashed line.

Monte Carlo simulation using the local constraints described above was thus carried out [see ref. (Withers et al., 2004) for details] and the corresponding electron diffraction patterns

calculated (Figs.5d-f) for comparison with the experimental ones shown in Figs.5a-c. From Fig. 5, it is clear that this local structure model fit very well with the observed electron diffraction data and gives a good idea of the local crystal chemistry. The constraints applied, as described above, were that the stoichiometry of each O'A_4 tetrahedron should be O'Bi_3Zn as far as possible, that $^1/_2$ <110> type Zn-Zn separation vectors be avoided as far as possible and finally that the Bi-Zn separation distances within each tetrahedron should be smaller than the average while the Bi-Bi distances should be larger than the average.

In summary, structured diffuse scattering provides clear evidence for crystal chemically sensible, local short range ordering of Bi and Zn ions and associated strain induced structural relaxation in cubic BZN pyrochlores. The experimentally observed diffuse distribution is dominated by the displacive shifts of the Bi and Zn ions on the pyrochore *A* sites of the O'A_2 sub-structure induced by local Bi/Zn ordering. While such induced displacive shifts do create local dipole moments (see Fig.6 above), these dipoles arise from local metal ion ordering and would therefore be expected to be static at room temperature (and therefore not responsible for the observed dynamic dielectric relaxation behaviour) unless there are a certain percentage of vacancies on the pyrochlore *A* site enabling the remaining *A* site metal ions to dynamically re-distribute themselves if the energy barriers to such motion are not too high.

2.1.2 'Non-stoichiometry' and the nature of defects in BZN (Liu et al., 2011)

While the above model provides a good fit to the observed structured diffuse scattering of BZN, there remain other sources of potential disorder arising from the intrinsic non-stoichiometry of BZN that should also be considered from the dielectric properties point of view. Levin *et al* (Levin et al., 2002) for example, found the composition of their BZN sample to be $(Bi_{1.5}Zn_{0.42})(Zn_{0.50}Nb_{1.5})O_{\sim 6.92}$. We have also synthesized 'non-stoichiometric' BZN samples as reported previously (Withers et al., 2004). It is thus clear that a small percentage of *A* site vacancies (Zn deficiency on the pyrochlore *A* site) and associated oxygen vacancies always co-exist (Levin et al., 2002; Withers et al., 2004; Levin et al., 2002a) in BZN pyrochlores and that the nominally ideal $(Bi_{1.5}Zn_{0.5})(Zn_{0.5}Nb_{1.5})O_7$ composition for BZN does not actually exist. How might this affect dielectric properties? As mentioned above, such non-stoichiometry might allow for local changes in the Bi/Zn/vacancy distribution and associated structural relaxation and hence changes in the local dipole distribution. On the other hand, one would expect any such re-distribution to occur on a rather slow time scale at room temperature.

An alternative possibility to explain dynamic dielectric relaxation behaviour is to consider the possibility of oxygen hopping and associated structural relaxation. This is best understood by considering the ideal pyrochlore structure type as a superstructure of the *Fm*3*m* fluorite structure type: six oxygens occupy the 48*f* sites therein and one is located in the 8*a* site per formula unit. The 8*b* site of the fluorite structure type, however, is nominally empty in an ideal pyrochlore [see refs. (Heremans et al., 1995; Moon etal., 1988) for details]. The existence of these vacant oxygen sites suggests the possibility of an exchange of an oxygen from the 48*f* site to this initially empty 8*b* interstitial site (Heremans et al., 1995; Moon et al., 1988). This creates a Frenkel defect denoted by $O_0 \leftrightarrow O_i^{''} + V_o^{\cdot\cdot}$ with a high activation energy between 1.54-1.70 eV(Tan et al., 2009; Clyton et al., 2001) due to the high level of intrinsic oxygen Frenkel disorder induced by the Zn deficiency and associated oxygen vacancies. The activation energy of such Frenkel defects is almost identical to a strong peak observed in the photoluminescence (PL) spectra of BZN (Liu et al, 2011),

suggesting a potential link between these two physical phenomena. Such an activation energy level (~1.67 eV) was also observed in (nominally) $Bi_{1.5}ZnSb_{1.5}O_7$, analogous to BZN, by Clayton *et al* (Clayton et al., 2001). The observed PL intensity is significantly reduced with increasing temperature due to the common PL quenching effect where non-radiative recombination is thermally activated and results in a decrease in the PL intensity. Once such a recombination occurs, the defects inducing the dipole moments vary and thus contribute to the observed dynamic dielectric relaxation. On the other hand, in the dilute limit, the concentration of defects then increases as a function of temperature (Kohan et al., 2000), which probably leads to an increase in the total number of defect-induced dipole moments and consequently to changes in the dielectric constant. This coincides with the trend observed in the dielectric-temperature spectra of BZN (Kamba et al., 2002). Volanti *et al* (Volanti et al., 2007) also suggest that oxygen vacancies and recombination of electrons and holes in the valence band lead to the formation of $[NbO_5 \cdot V_O^x]$, $[NbO_5 \cdot V_O^{\cdot}]$ and $[NbO_5 \cdot V_O^{\cdot\cdot}]$ *etc* complex clusters in the octahedral framework as donor, donor-acceptor and acceptor defects. The oxygen complex clusters generate localized states in the band gap and inhomogeneous charge distribution in the cell, and thus contribute to dielectric relaxation.

Taking all of these observations into account, it is apparent that Frenkel defects and associated defect clusters have a significant impact on the dielectric relaxation behaviour of BZN pyrochlores. Such Frenkel defects not only occur at high temperature but also can exist at much lower temperature if the BZN has an intrinsically significant numbers of vacancies on the *A* and O' sites.

2.2 Bi_2MNbO_7 (*M*=Fe^{3+}, In^{3+} and Sc^{3+}) pyrochlores

Now consider bismuth-rich niobate pyrochlores of nominal stoichiometry $Bi_2M^{III}NbO_7$ e.g. Bi_2FeNbO_7, Bi_2InNbO_7 and Bi_2ScNbO_7. Electron probe microanalysis showed the chemical compositions of the resultant compounds to be $Bi_{1.89}Fe_{1.16}Nb_{0.95}O_{6.95}$ (BFN), $Bi_{1.98}In_{0.99}Nb_{1.01}O_7$ (BIN) and $Bi_{1.99}Sc_{0.96}Nb_{1.03}O_7$ (BSN) respectively. BIN and BSN are thus cubic pyrochlores with only Bi in the pyrochlore *A* sites while BFN appears slightly Bi-deficient and to require a small amount (~5%) of Fe^{3+} ions on the pyrochlore *A* site as well as the Bi ions.

Figure 7 shows typical (a) <11-2> and (b) <22-3> zone axis EDPs of the $Bi_{1.89}Fe_{1.16}Nb_{0.95}O_{6.95}$ (BFN) sample. Note the presence of a highly structured diffuse intensity distribution, this time in the form of transverse polarized diffuse streaking in reciprocal space running through particular parent Bragg reflections perpendicular to each of the <110> directions of real space *e.g.* along <3-11>*, <1-3-1>* and <111>* in (a) and [10,-4,4]*, [-4,10, 4]* and [668]* in (b) [see ref. (Somphon et al., 2006) for detail]. Diffuse streaking of this type forms part of **G**±{110}* sheets of diffuse intensity in reciprocal space running perpendicular to each of the <110> directions of real space. Note that the diffuse streaking along the [668]* direction in Fig. 7b runs through the [*hkl*]*, *h–k = 4J*, *J* an integer, parent Bragg reflections e.g. [2-20]* but not through reflections [424]*. Likewise the diffuse streaking running along the [10, -4, 4]* direction runs through the [*hkl*]*, *k+l = 4J*, e.g. [244]* but not through reflections [424]*. Such characteristic pseudo-extinction conditions are characteristic of anti-cristobalite-type, orientational disorder of the O'Bi_4 tetrahedra (Tabira et al., 2001; Withers et al., 1989) that make up the O'A_2 sub-structure of the ideal pyrochlore structure type because of the correlated displacement of heavily scattering Bi ions separated by 1/4 <110> [see Fig. 8a and ref. (Somphon et al., 2006) for more detail].

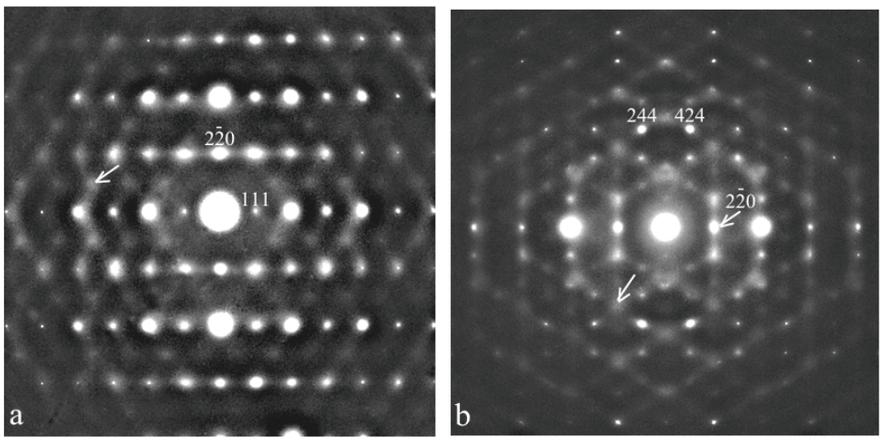

Fig. 7. Typical <11-2> and <22-3> zone axis electron diffraction patterns of BFN. See ref. (Somphon et al., 2006) for details.

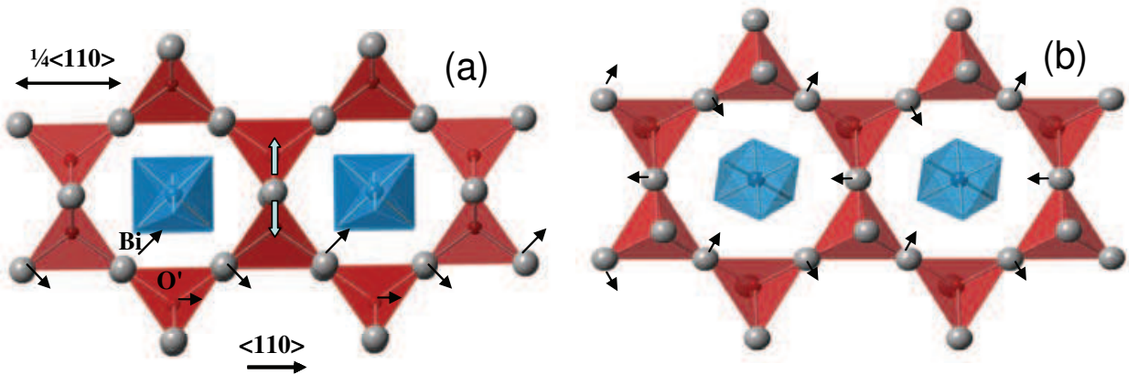

Fig. 8. (a) The characteristic anti-cristobalite-type displacive disorder of the O′Bi_2 sub-structure of the ideal pyrochlore structure type. The rotation of any one O′Bi_4 tetrahedron around the appropriate <1-10> tetrahedral edge automatically constrains all the tetrahedra in that particular <110> column to rotate but does not constrain the sense of tetrahedral rotation from one such <110> column to the next. Blue arrows indicates this Bi does not move. (b) the pattern of correlated O′Bi_4 tetrahedral rotation around the <111> axis responsible for the observed <111>* rods of diffuse intensity. Note that rotation of any O′Bi_4 tetrahedron around <111> automatically constrains all the tetrahedra in that particular <111> plane to rotate as shown in (a) but does not constrain the sense of tetrahedral rotation from one such <111> plane to the next. Note that each Bi ion moves essentially directly towards two of the O anions bonded to the B cations and directly away from two others.

The arrowed regions in Fig.7 show that virtual 'satellite reflections' in the form of quite distinct ''peaks'' in diffuse intensity arise whenever three diffuse streaks perpendicular to <110> intersect, e.g., at **G**±$^1/_2$[3-11]* ≡ **G**'±1/2[-1-11]* in Fig. 7a, and at **G**±(2J/7)[668]* ≡ **G**'±(2J/7[-1-11]* in Fig. 7b (J an integer). Such peaks in the diffuse intensity are part of essentially continuous 1-D rods of diffuse intensity running along the **G** ± <111>* directions of reciprocal space and imply the existence of correlated {111} planes of Bi displacements (shown in Fig. 8b) that are uncorrelated from one such {111} plane to the next.

The 'extinction conditions' characteristic of the {110}* sheets of diffuse intensity are also characteristic of the <111>* rods of diffuse intensity. This suggests that the displacive disorder responsible for these <111>* rods of diffuse intensity arises from an appropriate linear combination of tetrahedral edge rotations of the type shown in Fig.8a involving Bi displacements along the three <1-10> real space directions perpendicular to the particular <111>* rod of diffuse intensity and leading to resultant tetrahedral rotation around the <111> axis (as shown in Fig. 8b). According the analysis above, the mechanism adopted for local structural distortion away from the ideal pyrochlore structure type in BFN is clearly tetrahedral edge rotation of the O'A_2 sub-structure, either of the individual type shown in Fig.8a and/or of the correlated type shown in Fig. 8b.

Rather similar structured diffuse intensity distributions are also observed in the cases of BIN and BSN. Figure 9, for example, shows typical (a) <001> and (b) <11-2> zone axis electron diffraction patterns of BIN. Note the characteristic transverse polarized diffuse streaking perpendicular to the six <110> directions of real space *e.g.* along <220>* and <-220>* in (a) and along <3-11>* and <1-3-1>* in (b) *i.e.* the observed diffuse distribution again takes the form of sheets of diffuse intensity perpendicular to the six <110> directions of the average structure. As above, this again implies the existence of 1-D tetrahedral edge rotation of the O'A_2 tetrahedral sub-structure in BIN, in which the O'Bi_4 tetrahedra rotate as essentially rigid bodies with the O' remaining in the center of the tetrahedra (see Fig.8a above).

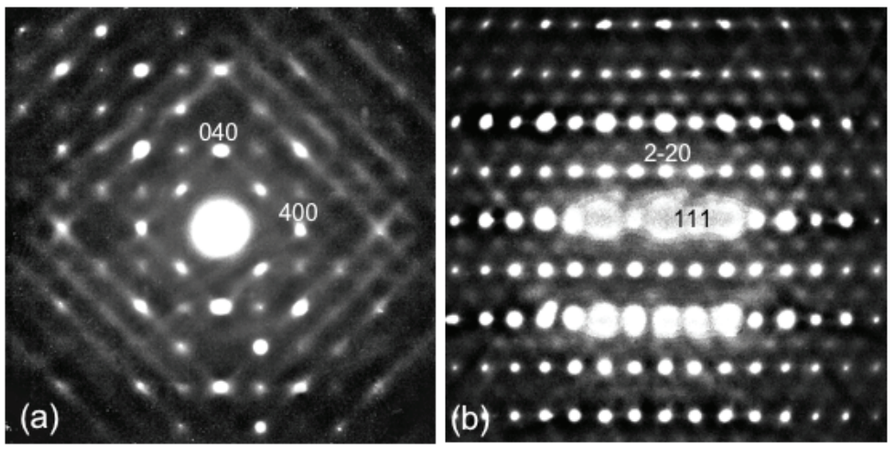

Fig. 9. Typical (a) <001> and (b) <11-2> zone axis electron diffraction patterns of BIN.

Figure 10 shows <-3,6,-1> (a) and (b) <5,1,-2> zone axis electron diffraction patterns of BSN. Again the characteristic, transverse polarized diffuse streaking running along a <*h*,-*h*, *l*>* direction of reciprocal space perpendicular to one or other of the six <110> directions of reciprocal space is clearly apparent *i.e.* the well-defined **G**±{110}* sheets of diffuse intensity also exist in the case of BSN as does the 1-D tetrahedral edge rotation of the O'A_2 tetrahedral sub-structure responsible.

According to the bond valence sum calculations based on the average structures of BFN, BIN and BSN (*e.g.* in Somphon et al., 2006), the O' anion co-ordinated to four Bi cations in the O'A_2 tetrahedral sub-structure is always over-bonded. The local O'-Bi bond lengths are thus happy to be slightly expanded as is achieved by large amplitude tetrahedral rotation of the type shown in Fig.8a. On the other hand, the significantly under-bonded Bi^{3+} ion cannot afford to lose much of the contribution to its bond valence arising from its two surrounding

O' ions. Therefore, the Bi ions must displace orthogonal to their local O'-Bi-O' axis and the $O'Bi_4$ tetrahedra must rotate and translate essentially as rigid units, as necessitated by the tetrahedral edge rotation patterns shown in Fig.8.

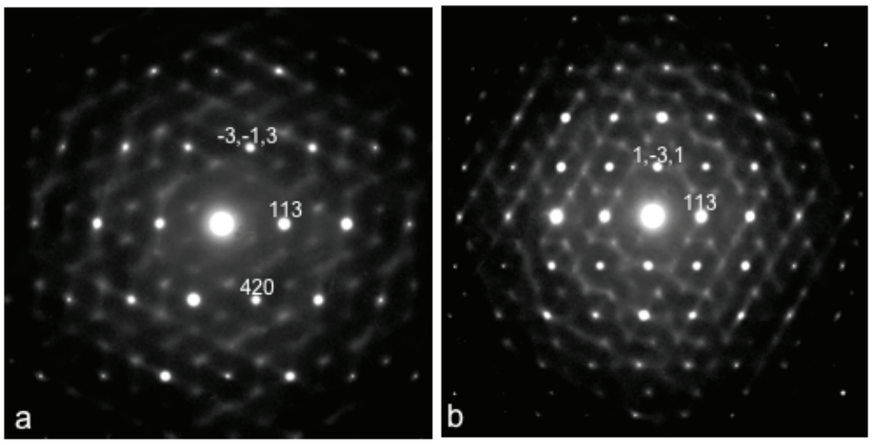

Fig. 10. Typical (a) <-36-1> and (b) <51-2> zone axis electron diffraction patterns of BSN.

The characteristic structured diffuse scattering observed in Figs. 7, 9 and 10 above (in the cases of BFN, BIN and BSN) arise from β-cristobalite-like, 1-d correlated rotations and associated translations along <110> of chains of corner-connected $O'Bi_4$ tetrahedra, as shown in Fig.8a above. It is important to note that the latter rigid body translation along <110> of a nominally +4 charged $O'Bi_2$ column of tetrahedra relative to the nominally -4 charged $M^{3+}Nb^{5+}O_6$ octahedral sub-structure, leads to a net dipole moment along the relevant <110> direction. The lack of transverse correlation from one such <110> chain to the next gives rise to the **G**±{110}* sheets of diffuse intensity. The observed structured diffuse distributions imply that such dipole moments exist along all six <110> directions, the local competition between the different possible polar directions presumably giving rise to the dielectric relaxation behaviour at low temperature and preventing the onset of long range hence ferroelectric ordering even at the lowest possible temperatures. By fitting experimental data to the measured temperature dependence of the dielectric spectra of BSN and BIN (Liu et al., 2009), reasonable activation energies, E_a, of 0.071 (0.072) eV and attempt jump frequencies of 6.48 (6.34) THz were obtained for BSN (BIN) respectively. We thus believe these intrinsically very low energy, correlated, chain rotation modes provide a key to understanding the structural origin of the dipoles as well as the slow dielectric relaxation behaviour of these Bi-based pyrochlores. On the other hand, it is noteworthy that the non-stoichiometry of BFN, like BZN, probably produces defect-induced dielectric relaxation behaviour like BZN.

2.3 BNN and BMN pyrochlores

Finally consider the cases of BNN and BMN of nominal stoichiometry $Bi_{1.5}MgNb_{1.5}O_7$ for BMN and $Bi_{1.5}NiNb_{1.5}O_7$ for BNN. Careful phase analysis shows that both of these systems are distinctly 'non-stoichiometric' with the as-synthesized materials having compositions of $(Bi_{0.833}Mg_{0.11}\square_{0.06})_2(Mg_{0.24}Nb_{0.76})_2O_7$ and $(Bi_{0.833}Ni_{0.125}\square_{0.04})_2(Ni_{0.25}Nb_{0.75})_2O_7$ (□ a vacancy) assuming no oxygen vacancies. In both cases, the Ni or Mg ions must occupy both the pyrochlore *A* and *B* sites while there are also significant concentration vacancies on the *A* sites, like BZN.

One might therefore expect a structured diffuse distribution like that observed above for BZN. Instead of this, in both cases structured diffuse distributions quite similar to those seen for BIN, BSN and BFN were observed *i.e.* transverse polarized diffuse streaking along the <*h*,-*h*,*l*>* directions of reciprocal space perpendicular to the six <110> directions of real space. Fig.11, for example, shows typical (a) <2,2,-3> and (b) close to <1,1,-2> zone axis electron diffraction patterns of BNN and BMN respectively. The observed highly structured diffuse distributions in both cases have distinct similarities to the structured diffuse distribution shown to be characteristic of BFN (Fig. 7), BIN (Fig.9) and BSN (Fig.10), and coincidentally, quite dissimilar to that characteristic of BZN.

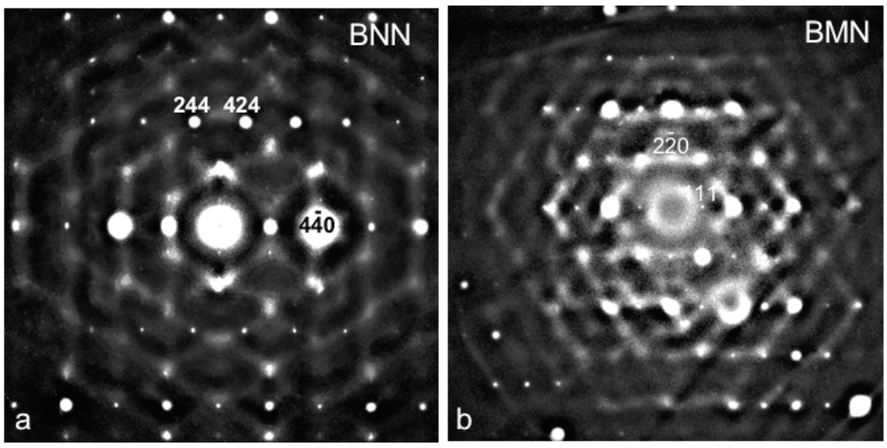

Fig. 11. Typical (a) <22-3> and (b) close to <11-2> zone axis electron diffraction patterns of BNN and BMN respectively.

Clearly the same β-cristobalite-like, 1-d correlated rotations and associated translations along <110> of chains of corner-connected $O'A_4$ tetrahedra must also be taking place in both BNN and BMN. However, when the concentration of the small, heavily under-bonded *M* = Mg or Ni on the pyrochlore A site is much more like 11–12% rather than the ~ 21% for BZN and where the concentration of □'s on the *A* sites is ~5%, the explanation for the observed highly anisotropic displacive disorder on the *A* site is not so obvious. The presence of ~5% □'s on the *A* sites, complicates matters considerably. When an O' ion is surrounded by either 4 Bi's of 3 Bi's and one Mg or Ni ion (the most likely local configurations), the centreing O' ion is either happily bonded or over-bonded implying that the significantly under-bonded Bi and heavily underbonded Mg or Ni ions cannot improve their under-bonding by moving closer to the O' ions but must instead move perpendicular to the local O'–A–O'-axis. When an O'ion is surrounded by 3 Bi's and one □ (a reasonably common likelihood), however, the centreing O' ion will be under-bonded and hence will move away from the □ and towards the remaining three Bi ions.

3. Chapter summary

All the above bismuth-based niobate pyroclores have the same displacively disordered *Fd-3m* average structure, as shown in Fig.2 above. The local structure of BZN as revealed by structured diffuse scattering, however, is quite different to the others. Two types of local order are observed in the studied pyrochlores:

1. Local (Bi/Zn) ordering on the O'A_2 sub-structure and associated displacive relaxation has been shown to give rise to the observed **G**±[10*l*]*, **G**±[*h*10]* and **G**±[0*k*1]* diffuse distribution. This diffuse distribution, however, is only observed in the case of BZN. One would not expect the metal ions to be mobile at room temperature, however, and hence this short range order is most probably not responsible for the dielectric relaxation that occurs at low temperature.
2. For the rest of the pyrochlores studied, **G**±{110}* sheets of diffuse intensity perpendicular to each of the six <110> directions of real space were observed implying that the same β-cristobalite-like, 1-d correlated rotations and associated translations along <110> of chains of corner-connected $O'A_4$ tetrahedra are taking place. It is important to note that the latter rigid body translation along <110> of a nominally +4 charged O'Bi_2 column of tetrahedra relative to the nominally -4 charged $M^{3+}Nb^{5+}O_6$ octahedral sub-structure, leads to a net dipole moment along the relevant <110> direction.
3. The observed {110}* diffuse sheets imply that these dipole moments exist along all six <110> directions simultaneously. The competition between these different local dipoles and their lifetimes may well be responsible for the observed dynamic dielectric relaxations. The low temperature peak in the dielectric loss tangent at T_m depends on the Bi content on the pyrochlore *A* site. The higher the Bi content, the higher T_m *i.e.* $T_{BZN}<T_{(BNN\ and\ BMN)}<T_{BFN}<T_{(BIN\ and\ BSN)}$.
4. The observed structured diffuse distribution is likely a widespread phenomenon in Bi-based pyrochlores and arises from their particular local crystal chemistry. The ratio of *M* to Bi on the pyrochlore A site plays an important role. The dielectric relaxation properties of such Bi-based niobate pyrochlores are dependent upon this local crystal chemistry.

4. Acknowledgment

The authors acknowledge financial support from the Australian Research Council (ARC) in the form of ARC Discovery Grants.

5. References

Brese N.E. and O'Keeffe M., (1991), Bond-valence paramters for solids, *Acta Cryst.B*, Vol 47, No 2, PP192. DOI: 10.1107/S0108768190011041

Butler B.D., Withers R.L. and Welberry T.R., (1992), Diffuse absences due to the atomic size effect, *Acta Cryst. A*, Vol 48, PP737. DOI: 10.1107/S0108767392003131

Clayton J., Takamura H., Metz R., Tuller H.L. and Wuensch B.J., (2001), The Electrical and Defect Properties of $Bi_3Zn_2Sb_3O_{14}$ Pyrochlore: A Grain-Boundary Phase in ZnO-Based Varistors, *J. Electroceram.*, Vol 7, PP113.

Heremans C., Wuensch B.J., Stalick J.K. and Prince E., (1995), Fast-Ion Conducting $Y_2(Zr_yTi_{1-y})_2O_7$ Pyrochlores: Neutron Rietveld Analysis of Disorder Induced by Zr Substitution, *J. solid state chem.*, Vol 117, No 1, PP108.

Kamba S., Porokhonskyy V., Pashkin A., Bovtun V., Petzel J., Nino J. Trolier-McKinstry C., S., Lanagan M.T., and Randall C.A., (2002), Anomalous broad dielectric relaxation in $Bi_{1.5}Zn_{1.0}Nb_{1.5}O_7$ pyrochlore, *Phys. Rev. B* , Vol 66, No 5, PP054106. DOI: 10.1103 /PhysRevB.66.054106

Kohan F., Ceder G., Morgan D. and Walle C.G.V.d., (2000), First-principles study of native point defects in ZnO, *Phys. Rev.B*, Vol 61, No 22, PP15019. DOI: 10.1103 /PhysRevB.61.15019

Levin I., Amos T.G., Nino J.C., Vanderah T.A., Randall C.A. and Lanagan M.T., (2002), Structural Study of an Unusual Cubic Pyrochlore $Bi_{1.5}Zn_{0.92}Nb_{1.5}O_{6.92}$, *J. Solid State Chem.,* Vol 168, No 1, PP69. doi:10.1006/jssc.2002.9681

Levin I., Amos T.G., Nino J.C., Vanderah T.A., Reaney I.M. and Randall C.A., (2002), Crystal Structure of the Compound $Bi_2Zn_{2/3}Nb_{4/3}O_7$, *J. Mater. Res.*, Vol 17, No 6, PP1406.

Liu Y., Withers R. L., Nguyen B. and Elliott K., (2009), Displacive disorder and dielectric relaxation in the stoichiometric bismuth-containing pyrochlores, $Bi_2M^{III}NbO_7$ (*M*=In and Sc), *J. Solid State Chem.*, Vol 182, No 10, PP2748. doi:10.1016 /j.jssc.2009.07.007

Liu Y., Withers R.L. and Wei X.Y., (2005), Structurally frustrated relaxor ferroelectric behavior in $CaCu_3Ti_4O_{12}$, *Phys. Rev. B*, Vol 72, No 13,PP134104. doi: 10.1103/ PhysRevB.72.134104

Liu Y., Withers R.L., Chen H., Li Q., and Tan H., (2011), Raman spectra, photoluminescence and dielectric relaxation in $Bi_{1.5}ZnNb_{1.5}O_7$ pyrochlore, *Curr. App. Phys.*, Vol xx, PP xxxx. doi:10.1016/j.cap.2011.03.014

Moon P.K. and Tuller H.L., (1988), Ionic conduction in the $Gd_2Ti_2O_7$–$Gd_2Zr_2O_7$ system , *Solid State Ionics*, Vol 28-30, No 1, PP470.

Nino J.C., Lanagan M.T., and Randall C.A., (2001), Dielectric relaxation in Bi_2O_3–ZnO–Nb_2O_5 cubic pyrochlore, *J. Appl. Phys.*, Vol 89, No 8, PP4512. doi:10.1063/1.1357468

Nguyena. H.B., Norén L., Liu Y., Withers R.L., Wei. X.Y. and Elcombe M.M., (2007a), The disordered structures and low temperature dielectric relaxation properties of two misplaced-displacive cubic pyrochlores found in the Bi_2O_3–$M^{II}O$–Nb_2O_5 (M=Mg, Ni) systems, *J. Solid State Chem.*, Vol 180, No 9, PP2558. doi:10.1016 /j.jssc.2007.07.003

Nguyen B., Liu Y., and Withers R.L., (2007b), The local crystal chemistry and dielectric properties of the cubic pyrochlore phase in the Bi_2O_3-$M^{2+}O$-Nb_2O_5 (M^{2+}=Ni^{2+} and Mg^{2+}) systems, *J. Solid State Chem.*, Vol 180, No 2, PP549. doi:10.1016 /j.jssc.2006.10.039

Somphon W., Ting V., Liu Y., Withers R.L., Zhou Q. and Kennedy B.J., (2006), Local crystal chemistry, structured diffuse scattering and the dielectric properties of $(Bi_{1-x}Y_x)_2(M^{III}Nb^V)O_7$ (M=Fe^{3+}, In^{3+}) Bi-pyrochlores, *J. Solid State Chem.*, Vol 179, No 8 PP2495. doi:10.1016/j.jssc.2006.04.046

Tabira Y., Withers R.L. , Yamada T. and Ishizawa N. , (2001), Annular dynamical disorder of the rare earth ions in a $La_2Zr_2O_7$ pyrochlore via single crystal synchrotron X-ray diffraction, *Z. Krist.*, Vol 216, No 2, PP92.

Tan K.B., Khaw C.C., Lee C.K., Zainal Z., Tan Y.P. and Shaari H., (2009), High temperature impedance spectroscopy study of non-stoichiometric bismuth zinc niobate pyrochlore, *Materials Science-Poland*, Vol 27, No 3, PP825.

Volanti D.P., Cavalcante L.S., Paris E.C., Simões A.Z., Keyson D., Longo V.M., Figueiredo A.T.d., Longo E., and Varela J.A., (2007), Photoluminescent behavior of $SrBi_2Nb_2O_9$ powders explained by means of β-Bi_2O_3 phase, *Appl. Phys.Lett.*, Vol 90, No 26, PP261913. doi:10.1063/1.2753114

Withers R.L., Welberry T.R., Larsson A.-K., Liu Y., Norén L., Rundlöf H. and Brink F. J., (2004), Local crystal chemistry, induced strain and short range order in the cubic pyrochlore $(Bi_{1.5-\alpha}Zn_{0.5-\beta})(Zn_{0.5-\gamma}Nb_{1.5-\delta})O_{(7-1.5\alpha-\beta-\gamma-2.5\delta)}$ (BZN) , *J. Solid State Chem.*, Vol 177, No 1, PP231. doi:10.1016/j.jssc.2003.07.005

Withers, R.L., Thompson J.G. and Welberry T.R., (1989), The structure and microstructure of α-cristobalite and its relationship to β-cristobalite, Phys. Chem. Miner., Vol 16, No 6, PP 517.

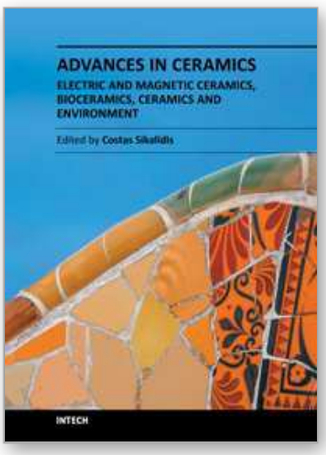

Advances in Ceramics - Electric and Magnetic Ceramics, Bioceramics, Ceramics and Environment

Edited by Prof. Costas Sikalidis

ISBN 978-953-307-350-7
Hard cover, 550 pages
Publisher InTech
Published online 06, September, 2011
Published in print edition September, 2011

The current book consists of twenty-four chapters divided into three sections. Section I includes fourteen chapters in electric and magnetic ceramics which deal with modern specific research on dielectrics and their applications, on nanodielectrics, on piezoceramics, on glass ceramics with para-, anti- or ferro-electric active phases, of varistors ceramics and magnetic ceramics. Section II includes seven chapters in bioceramics which include review information and research results/data on biocompatibility, on medical applications of alumina, zirconia, silicon nitride, ZrO2, bioglass, apatite-wollastonite glass ceramic and b-tri-calcium phosphate. Section III includes three chapters in applications of ceramics in environmental improvement and protection, in water cleaning, in metal bearing wastes stabilization and in utilization of wastes from ceramic industry in concrete and concrete products.

How to reference

In order to correctly reference this scholarly work, feel free to copy and paste the following:

Yun Liu and Ray L. Withers (2011). Local Structure of Relaxor Dielectric Ceramics, Advances in Ceramics - Electric and Magnetic Ceramics, Bioceramics, Ceramics and Environment, Prof. Costas Sikalidis (Ed.), ISBN: 978-953-307-350-7, InTech, Available from: http://www.intechopen.com/books/advances-in-ceramics-electric-and-magnetic-ceramics-bioceramics-ceramics-and-environment/local-structure-of-relaxor-dielectric-ceramics

INTECH
open science | open minds

InTech Europe
University Campus STeP Ri
Slavka Krautzeka 83/A
51000 Rijeka, Croatia
Phone: +385 (51) 770 447
Fax: +385 (51) 686 166
www.intechopen.com

InTech China
Unit 405, Office Block, Hotel Equatorial Shanghai
No.65, Yan An Road (West), Shanghai, 200040, China
中国上海市延安西路65号上海国际贵都大饭店办公楼405单元
Phone: +86-21-62489820
Fax: +86-21-62489821

IntechOpen